Eighth International Conference on
THIN-WALLED STRUCTURES – ICTWS 2018
Lisbon, Portugal, July 24-27, 2018

A GEOMETRICALLY EXACT KIRCHHOFF BEAM FINITE ELEMENT WITH TORSION WARPING

David Manta* and Rodrigo Gonçalves*

* CERIS and Departamento de Engenharia Civil, Faculdade de Ciências e Tecnologia
Universidade Nova de Lisboa 2829-516 Caparica, Portugal
e-mails: d.manta@campus.fct.unl.pt, rodrigo.goncalves@fct.unl.pt

Keywords: Geometrically exact beams; Kirchhoff beams; Torsion warping; Beam finite elements.

Abstract. *In this paper, a geometrically exact beam model is presented that includes the Kirchhoff constraint and torsion-related warping, aiming at capturing accurately the flexural-torsional behaviour of slender thin-walled beams undergoing large displacements. The cross-section rotation tensor is obtained from two successive rotations: a torsional rotation and a smallest rotation to the tangent vector of the beam axis. Noteworthy aspects of the proposed formulation are the following: (i) the equilibrium equations and their linearization are completely written in terms of the independent kinematic parameters, (ii) torsion-warping is allowed, as well as Wagner effects, and (iii) arbitrary cross-sections are considered, namely cross-sections where the shear centre and centroid do not coincide. The accuracy and computational efficiency of the finite element implementation of the proposed model is demonstrated in several numerical examples involving large displacements.*

1 INTRODUCTION

Geometrically exact beam models usually describe the cross-section position independently of its orientation, as in the pioneering works of Reissner [2,3] and Simo [4], and subsequently followed by many authors (e.g., [5–11]). However, for slender beams, shear deformation may be discarded (the Kirchhoff constraint) and the cross-section orientation becomes constrained to the tangent vector of the beam axis. The advantages of employing this constraint are twofold: (i) the number of kinematic DOFs are reduced and (ii) shear locking problems are discarded *a priori*. However, on the other hand, the fact that the cross-section rotation is constrained complicates the kinematic relations.

The first 3D geometrically exact Kirchhoff elastic beam formulations are relatively recent [12,13,1] and concern initially straight beams with circular cross-section, in which case it is not necessary to keep track of the cross-section in-plane axes. In [1], two successive rotations were used to parametrize the cross-section rotation: a torsional rotation and the so-called smallest rotation [14], which aligns the normal to the cross-section with the beam axis tangent. In [15] this parametrization was employed in a geometrically exact thin-walled beam finite element incorporating the Kirchhoff and Vlasov constraints (null shear and bi-shear deformation), as well as arbitrary cross-section in-plane and out-of-plane (warping) deformation, to perform linear stability analyses. The planar case (Euler-Bernoulli) has also been addressed in the past (e.g., [16,17]) and, in [18], a materially non-linear finite element was proposed and employed to study the buckling behaviour of steel-concrete composite columns. In [19], a Kirchhoff element was proposed which can handle initially curved geometries and more general cross-sections, whose centroid and shear centre coincide. It was shown that the smallest rotation parametrization leads to non-objectivity and therefore a new parametrization of the cross-section rotation was proposed, where the rotation within each element is obtained from those of the end node cross-sections. This formulation proved to be objective and path-independent.

The present paper presents a geometrically exact Kirchhoff beam model that captures the flexural-torsional behavior of thin-walled beams undergoing large displacements. Torsion-warping and Wagner effects are allowed for, as well as cross-sections with non-coincident shear center and centroid. A finite element is obtained by approximating the independent kinematic parameters using Hermite cubic functions. The kinematic description of the beam is similar to that introduced in [20], including (i) a warping DOF to allow for an accurate representation of the torsional behavior, namely the Wagner effect, and (ii) the Kirchhoff constraint. It should be noted that the present model is not concerned with arbitrarily large displacements, as emphasis is given to the assessment of the smallest rotation parametrization approach and its application to capture flexural-torsional deformation in thin-walled beams. In this context, the singularity of the parametrization, occurring for a rotation equal to π, is not approached and a path-independent (although non-objective) formulation is obtained.

For the notation, scalars are represented by *italic* letters, whereas second-order tensors, vectors and matrices are represented by ***bold italic*** letters. The derivatives with respect to the coordinates X_i (i=1,2) are indicated by $(\cdot)_{,i}$, and the derivative with respect to X_3 is represented by a prime $(\cdot)'$. Virtual and incremental/iterative variations are denoted by δ and Δ, respectively. The tilde $\tilde{\boldsymbol{a}}$ indicates a skew-symmetric second order tensor whose axial vector is $\boldsymbol{a}$. The standard tensor, vector and scalar products between two vectors $\boldsymbol{a}$ and $\boldsymbol{b}$ are indicated by $\boldsymbol{a}\otimes\boldsymbol{b}$, $\boldsymbol{a}\times\boldsymbol{b}$ and $\boldsymbol{a}\cdot\boldsymbol{b}$, respectively, and the vector norm is $\|\boldsymbol{a}\|=\sqrt{\boldsymbol{a}\cdot\boldsymbol{a}}$.

2 THE GEOMETRICALLY EXACT THIN-WALLED BEAM MODEL

2.1 Kinematic description

Let (X_1, X_2, X_3) define an orthonormal direct reference system, with base vectors $\boldsymbol{E}_i$ (i=1,2,3), where the X_3 axis defines the beam initial longitudinal axis, coinciding with the line of cross-section shear centers C (the beam is initially straight). According to Figure 1, the initial configuration is defined by the position vector of each material point $\boldsymbol{X} = X_1\,\boldsymbol{E}_1 + X_2\,\boldsymbol{E}_2 + X_3\,\boldsymbol{E}_3$, with $X_3 \in [0, L]$, where L is the beam length, and X_1, X_2 lie on the cross-section and do not necessarily define principal axes.

For the deformed configuration, the position vector of each point is given by as

$$\boldsymbol{x}(X_1, X_2, X_3) = \boldsymbol{r}(X_3) + \boldsymbol{\Lambda}(X_3)\boldsymbol{l}\,, \tag{1}$$

where vector $\boldsymbol{r}$ references the cross-section center C, $\boldsymbol{\Lambda}$ is the cross-section orthogonal rotation tensor about C and $\boldsymbol{l}$ references each cross-section point with respect to C in the co-rotational frame $\boldsymbol{\Lambda E}_i$, reading

$$\boldsymbol{l} = X_1\boldsymbol{E}_1 + X_2\boldsymbol{E}_2 + \omega(X_1, X_2)\,p(X_3)\boldsymbol{E}_3\,, \tag{2}$$

where ω is the torsion-related warping function and p is its scalar weight function.

With the Kirchhoff constraint, with null warping (p = 0), the cross-section remains perpendicular to the beam axis and the rotation tensor satisfies

$$\boldsymbol{\Lambda E}_3 = \boldsymbol{t}\,, \tag{3}$$

where $\boldsymbol{t}$ is the unit tangent vector of the beam axis, defined as

$$\boldsymbol{t} = \frac{\boldsymbol{r}'}{\|\boldsymbol{r}'\|}. \tag{4}$$

The parametrization of the rotation tensor that satisfies Eq. (3) is discussed in Section 3.

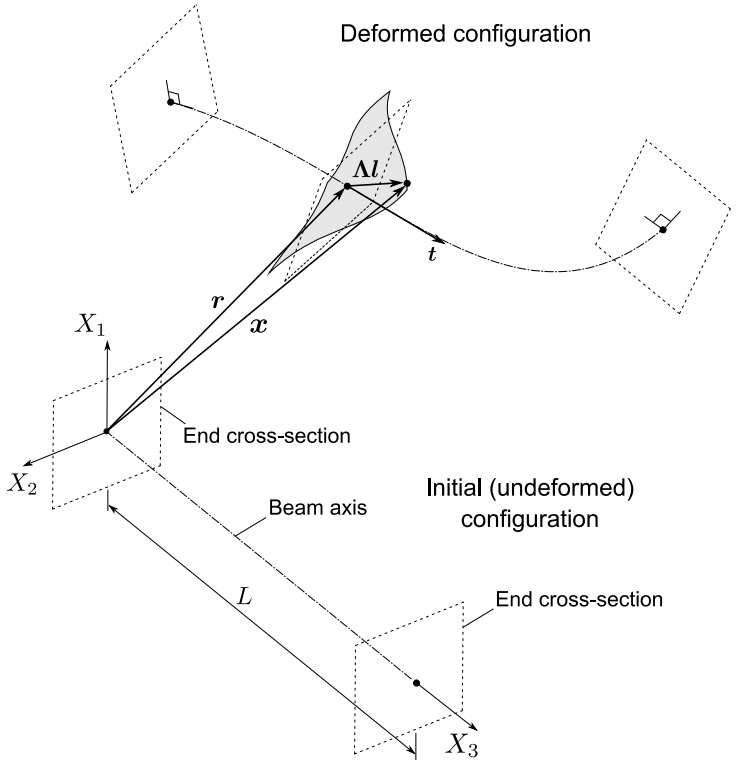

Figure 1: Initial and deformed configurations of the beam.

2.2 Strain

The standard deformation gradient $\boldsymbol{F} = \nabla \boldsymbol{x}$ is first written as follows

$$\boldsymbol{F} = \boldsymbol{\Lambda}(\boldsymbol{g}_1 \otimes \boldsymbol{E}_1 + \boldsymbol{g}_2 \otimes \boldsymbol{E}_2 + \boldsymbol{g}_3 \otimes \boldsymbol{E}_3)\,, \tag{5}$$

where $\boldsymbol{g}_i = \boldsymbol{\Lambda}^T \boldsymbol{F}\boldsymbol{E}_i$ are the back-rotations of the base vector push-forwards, $\boldsymbol{F}\boldsymbol{E}_i$. From Eqs. (1) and (2), these vectors are given by

$$\boldsymbol{g}_1 = \boldsymbol{E}_1 + \omega_{,1} p \boldsymbol{E}_3\,, \tag{6}$$

$$\boldsymbol{g}_2 = \boldsymbol{E}_2 + \omega_{,2} p \boldsymbol{E}_3\,, \tag{7}$$

$$\boldsymbol{g}_3 = \boldsymbol{\Gamma} + \boldsymbol{E}_3 + \boldsymbol{K} \times \boldsymbol{l} + \omega p' \boldsymbol{E}_3\,, \tag{8}$$

where the material strain measures introduced by Simo [4] have been employed, reading

$$\boldsymbol{\Gamma} = \boldsymbol{\Lambda}^T \boldsymbol{r}' - \boldsymbol{E}_3\,, \tag{9}$$

$$\boldsymbol{K} = \mathrm{axi}(\boldsymbol{\Lambda}^T \boldsymbol{\Lambda}')\,, \tag{10}$$

with $\boldsymbol{\Gamma}$ relating to the beam axis extension/shearing and $\boldsymbol{K}$ measuring its curvature.

Using Eqs. (3) and (4), only the extensional component (along $\boldsymbol{E}_3$) of $\boldsymbol{\Gamma}$ is non-null, as one obtains

$$\boldsymbol{\Gamma} = \boldsymbol{\Lambda}^T \boldsymbol{r}' - \boldsymbol{E}_3 = \boldsymbol{\Lambda}^T \boldsymbol{t} \,\|\, \boldsymbol{r}' \,\| - \boldsymbol{E}_3 = (\| \boldsymbol{r}' \| - 1)\boldsymbol{E}_3\,. \tag{11}$$

The Green-Lagrange strains $\boldsymbol{E} = \frac{1}{2}(\boldsymbol{F}^T\boldsymbol{F} - \boldsymbol{1})$ are obtained from the previous relations. The relevant components can be cast in a Voigt-like vector form as

$$\boldsymbol{E} = \begin{bmatrix} E_{33} \\ 2E_{31} \\ 2E_{32} \end{bmatrix} = \begin{bmatrix} \frac{1}{2}(\boldsymbol{g}_3 \cdot \boldsymbol{g}_3 - 1) \\ \boldsymbol{g}_1 \cdot \boldsymbol{g}_3 \\ \boldsymbol{g}_2 \cdot \boldsymbol{g}_3 \end{bmatrix}. \tag{12}$$

2.3 Equilibrium equations and their linearization

From the virtual work principle, using Green-Lagrange strains $\boldsymbol{E}$ and second Piola-Kirchhoff stresses $\boldsymbol{S}^T = [S_{33}\ S_{31}\ S_{32}]$, the equilibrium equations are obtained, reading

$$\delta W_{int} + \delta W_{ext} = 0\,, \tag{13}$$

$$\delta W_{int} = -\int_V \boldsymbol{S} \cdot \delta \boldsymbol{E}\ \mathrm{d}V\,, \tag{14}$$

$$\delta W_{ext} = \delta \boldsymbol{u} \cdot \boldsymbol{Q} + \delta \boldsymbol{\varpi} \cdot \boldsymbol{M}\,, \tag{15}$$

where V is the beam initial volume, $\boldsymbol{Q}$ is a concentrated force and $\boldsymbol{u} = \boldsymbol{x} - \boldsymbol{X}$ is its work--conjugate displacement, $\boldsymbol{M}$ is a concentrated moment about fixed axes and $\delta\boldsymbol{\varpi}$ is the spatial spin vector (see, e.g., [21]), given by

$$\widetilde{\delta\boldsymbol{\varpi}} = \delta\boldsymbol{\Lambda}\boldsymbol{\Lambda}^T\,. \tag{16}$$

The virtual variation of the strains is given by

$$\delta \boldsymbol{E} = \begin{bmatrix} \delta\boldsymbol{g}_3 \cdot \boldsymbol{g}_3 \\ \delta\boldsymbol{g}_1 \cdot \boldsymbol{g}_3 + \boldsymbol{g}_1 \cdot \delta\boldsymbol{g}_3 \\ \delta\boldsymbol{g}_2 \cdot \boldsymbol{g}_3 + \boldsymbol{g}_2 \cdot \delta\boldsymbol{g}_3 \end{bmatrix}. \tag{17}$$

A linear constitutive law is assumed between $\boldsymbol{S}$ and $\boldsymbol{E}$, reading

$$\boldsymbol{S} = \boldsymbol{C}\boldsymbol{E} = \begin{bmatrix} E & & \\ & G & \\ & & G \end{bmatrix} \boldsymbol{E}\,, \tag{18}$$

where E is Young's modulus and G is the shear modulus.

The incremental/iterative linearization of the virtual work equation reads

$$\Delta\delta W_{int} = -\int_V (\boldsymbol{S} \cdot \Delta\delta\boldsymbol{E} + \Delta\boldsymbol{E} \cdot \boldsymbol{C}\delta\boldsymbol{E})\ \mathrm{d}V\,, \tag{19}$$

$$\Delta\delta W_{ext} = \Delta\delta\boldsymbol{u} \cdot \boldsymbol{Q} + \Delta\delta\boldsymbol{\varpi} \cdot \boldsymbol{M}\,. \tag{20}$$

In Section 4, these equations are written explicitly in terms of the independent kinematic parameters, which follow from the choice of the cross-section rotation parametrization, discussed in the next Section.

3. PARAMETRIZATION OF THE CROSS-SECTION ROTATION

3.1 The cross-section rotation

As proposed in [1], the cross-section rotation tensor $\boldsymbol{\Lambda}$ is obtained from the composition of two successive rotations

$$\boldsymbol{\Lambda} = \boldsymbol{\Lambda}_t \boldsymbol{\Lambda}_\varphi \,. \tag{21}$$

The first rotation $\boldsymbol{\Lambda}_\varphi$ consists of a torsion rotation and may be parametrized using a rotation vector $\varphi \boldsymbol{E}_3$, where φ is the rotation angle. Using the Rodrigues formula (see, e.g., [23]), this leads to

$$\boldsymbol{\Lambda}_\varphi = \sin\varphi \tilde{\boldsymbol{E}}_3 + \cos\varphi(\boldsymbol{1} - \boldsymbol{E}_3 \otimes \boldsymbol{E}_3) + \boldsymbol{E}_3 \otimes \boldsymbol{E}_3 \,. \tag{22}$$

The second rotation $\boldsymbol{\Lambda}_t$ corresponds to the smallest rotation between $\boldsymbol{E}_3$ and $\boldsymbol{t}$ which, as shown in Figure 2(a), may be represented by a path along the geodesic that connects the two vectors (in the figure, the corresponding rotation vector is $\boldsymbol{\theta}$). This rotation tensor may be given by two alternative expressions [14]

$$\boldsymbol{\Lambda}_t = t_3 \boldsymbol{1} + \widetilde{\boldsymbol{E}_3 \times \boldsymbol{t}} + \frac{(\boldsymbol{E}_3 \times \boldsymbol{t}) \otimes (\boldsymbol{E}_3 \times \boldsymbol{t})}{1 + t_3} \,, \tag{23}$$

$$\boldsymbol{\Lambda}_t = \boldsymbol{1} + \widetilde{\boldsymbol{E}_3 \times \boldsymbol{t}} + \frac{(\widetilde{\boldsymbol{E}_3 \times \boldsymbol{t}})\,(\widetilde{\boldsymbol{E}_3 \times \boldsymbol{t}})}{1 + t_3} \,. \tag{24}$$

This parametrization is singular at $\boldsymbol{t} = -\boldsymbol{E}_3$, corresponding to a rotation $\|\boldsymbol{\theta}\| = \pi$, which is of minor relevance for the problems addressed in this paper, as previously mentioned.

3.1 Curvatures and spin

From (10), the axis curvature may be decomposed as follows

$$\boldsymbol{K} = \mathrm{axi}(\boldsymbol{\Lambda}_\varphi^T \boldsymbol{\Lambda}_t^T (\boldsymbol{\Lambda}'_t \boldsymbol{\Lambda}_\varphi + \boldsymbol{\Lambda}_t \boldsymbol{\Lambda}'_\varphi)) = \boldsymbol{\Lambda}_\varphi^T \boldsymbol{K}_t + \boldsymbol{K}_\varphi \,, \tag{25}$$

$$\boldsymbol{K}_t = \mathrm{axi}(\boldsymbol{\Lambda}_t^T \boldsymbol{\Lambda}'_t) \,, \tag{26}$$

$$\boldsymbol{K}_\varphi = \mathrm{axi}(\boldsymbol{\Lambda}_\varphi^T \boldsymbol{\Lambda}'_\varphi) = \varphi' \boldsymbol{E}_3 \,, \tag{27}$$

where the relation $(\boldsymbol{\Lambda}\, \tilde{\boldsymbol{a}}\, \boldsymbol{\Lambda}^T) = \boldsymbol{\Lambda}\, \boldsymbol{a}$ was used ($\boldsymbol{a}$ is an arbitrary vector) and φ' represents the torsion curvature due to φ. The derivation of an explicit expression for $\boldsymbol{K}_t$ is not straightforward. After several manipulations [26], one arrives at

$$\boldsymbol{K}_t = (\boldsymbol{K}_t)_B + K_{t3} \boldsymbol{E}_3 = \left(\boldsymbol{1} - \frac{(\boldsymbol{t} + 2\boldsymbol{E}_3) \otimes \boldsymbol{E}_3}{1 + t_3} \right) (\boldsymbol{t} \times \boldsymbol{t}') \,, \tag{28}$$

where the bending and torsion components are given by

$$(\boldsymbol{K}_t)_B = \boldsymbol{t}\times\boldsymbol{t}' - \frac{\boldsymbol{E}_3\cdot(\boldsymbol{t}\times\boldsymbol{t}')}{1+t_3}(\boldsymbol{t}+\boldsymbol{E}_3), \tag{29}$$

$$K_{t3} = -\frac{(\boldsymbol{t}\times\boldsymbol{t}')\cdot\boldsymbol{E}_3}{1+t_3}. \tag{30}$$

Note that (30) shows that torsion curvature is developed if $(\boldsymbol{t}\times\boldsymbol{t}')\cdot\boldsymbol{E}_3 \neq 0$, which occurs if $\boldsymbol{t}'$ does not lie in the plane defined by $\boldsymbol{t}$ and $\boldsymbol{E}_3$, i.e., if there is a change in the geodesic between adjacent cross-sections. The total torsion curvature is given by the sum of (27) and (30). For illustrative purposes, Fig. 2(b) shows the evolution of the cross-section triad $\boldsymbol{\Lambda}_t\boldsymbol{E}_i$ for two distinct configurations of a 10 m length beam, which have the same end cross-section tangents and are characterized by $\varphi = 0$. Path I corresponds to $\boldsymbol{r} = (X_3^2/2L)\boldsymbol{E}_1 - (X_3^2/L)\boldsymbol{E}_2 + X_3\boldsymbol{E}_3$ and in this case $\boldsymbol{t}'$ travels along a geodesic, not inducing torsional curvature. Path II is given by $\boldsymbol{r} = (X_3^3/3L^2)\boldsymbol{E}_1 - (X_3^2/L)\boldsymbol{E}_2 + X_3\boldsymbol{E}_3$ and generates torsional curvature, as shown in the graph.

Note that K_{t3} generally changes under rigid-body rotations. As pointed out in [19], although φ could be prescribed to compensate for the change in K_{t3} due to the rigid-body rotation, Eq. (30) is a rather complex function and cannot be accurately matched by a standard interpolation of φ, rendering the formulation non-objective. Nevertheless, this problem is reduced as the finite element length is decreased and/or the interpolation functions of φ are enhanced.

As for the spatial spin, from the rotation, by $\boldsymbol{\Lambda}$, of (27), (29) and (30) and changing the derivative, one obtains

$$\delta\boldsymbol{\varpi} = \boldsymbol{t}\times\delta\boldsymbol{t} - \frac{(\boldsymbol{t}\times\delta\boldsymbol{t})\cdot\boldsymbol{E}_3}{1+t_3}\boldsymbol{t} + \delta\varphi\boldsymbol{t}. \tag{31}$$

4. A TWO-NODE BEAM FINITE ELEMENT

The finite element implementation of the proposed formulation is obtained by interpolating the displacement of the beam axis $\boldsymbol{r} - X_3\boldsymbol{E}_3$, the rotation φ and the warping weight function p. The independent kinematic parameters are collected in vector $\boldsymbol{\phi}$, as follows

$$\boldsymbol{\phi} = \begin{bmatrix} \boldsymbol{r} \\ \varphi \\ p \end{bmatrix}. \tag{32}$$

Due to the Kirchhoff constraint, slope continuity is required for the displacement of the beam axis and thus standard Hermite cubic functions are employed. Although this is not required for φ and p, the same functions are employed. This leads to a two-node beam finite element with 10 DOFs per node. The equilibrium equations are solved with a standard incremental/iterative scheme with load/displacement control. Numeric integration is carried out with three Gauss points along X_3, to avoid membrane locking, as in [1]. For thin-walled cross-sections, integration is performed using a 3×3 Gauss point grid in each wall.

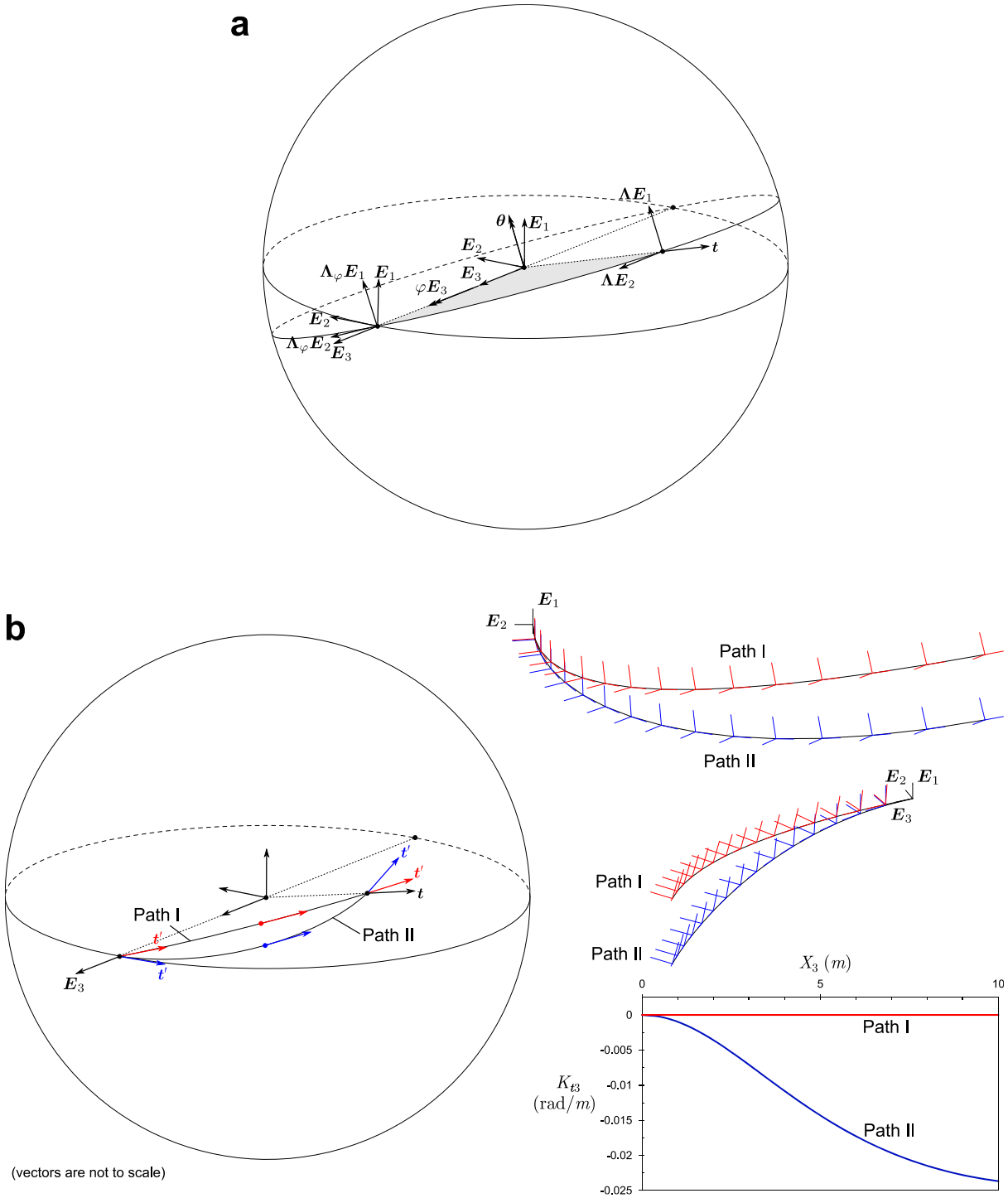

Figure 2: (a) Parametrization of the cross-section rotation and (b) evolution of the cross-section orientation along two paths with coinciding end tangents (path II yields torsion curvature).

The equilibrium equations and their linearization are written in terms of the kinematic parameters in $\boldsymbol{\phi}$ using auxiliary matrices $\boldsymbol{\Xi}_{(\cdot)}$ and $\boldsymbol{\Theta}_{(\cdot)}$, as in [10,11]. The complete and detailed expressions are given in [26]. Furthermore, the following vector is defined

$$\boldsymbol{\Phi} = \begin{bmatrix} \boldsymbol{\phi} \\ \boldsymbol{\phi}' \\ \boldsymbol{\phi}'' \end{bmatrix}, \tag{33}$$

as the equations are written in terms of $\delta\boldsymbol{\Phi}$ and $\Delta\boldsymbol{\Phi}$. In particular, the internal virtual work (14) may be written as

$$\delta W_{int} = -\int_V \delta\boldsymbol{\Phi}^T \boldsymbol{\Xi}_{D\boldsymbol{E}}^T \; \boldsymbol{S} \; \mathrm{d}V \,, \tag{34}$$

$$\boldsymbol{\Xi}_{D\boldsymbol{E}} = \begin{bmatrix} [\boldsymbol{g}_3]^T \boldsymbol{\Theta}_{D\boldsymbol{g}_3} \\ [\boldsymbol{g}_1]^T \boldsymbol{\Theta}_{D\boldsymbol{g}_3} + [\boldsymbol{g}_3]^T \boldsymbol{\Theta}_{D\boldsymbol{g}_1} \\ [\boldsymbol{g}_2]^T \boldsymbol{\Theta}_{D\boldsymbol{g}_3} + [\boldsymbol{g}_3]^T \boldsymbol{\Theta}_{D\boldsymbol{g}_2} \end{bmatrix}. \tag{35}$$

Its linearization reads

$$\Delta\delta W_{int} = -\int_V \delta\boldsymbol{\Phi}^T (\boldsymbol{\Xi}_{D\boldsymbol{E}}^T \; \boldsymbol{C} \; \boldsymbol{\Xi}_{D\boldsymbol{E}} + \boldsymbol{\Xi}_{D^2\boldsymbol{E}}(\boldsymbol{S}))\Delta\boldsymbol{\Phi} \; \mathrm{d}V \,, \tag{36}$$

$$\begin{aligned} \boldsymbol{\Xi}_{D^2\boldsymbol{E}}(\boldsymbol{S}) = {} & S_{33}\left(\boldsymbol{\Theta}_{D\boldsymbol{g}_3}^T \boldsymbol{\Theta}_{D\boldsymbol{g}_3} + \boldsymbol{\Theta}_{D^2\boldsymbol{g}_3}(\boldsymbol{g}_3)\right) + S_{13}\left(\boldsymbol{\Theta}_{D\boldsymbol{g}_1}^T \boldsymbol{\Theta}_{D\boldsymbol{g}_3} + \boldsymbol{\Theta}_{D\boldsymbol{g}_3}^T \boldsymbol{\Theta}_{D\boldsymbol{g}_1} + \boldsymbol{\Theta}_{D^2\boldsymbol{g}_3}(\boldsymbol{g}_1)\right) \\ & + S_{23}\left(\boldsymbol{\Theta}_{D\boldsymbol{g}_2}^T \boldsymbol{\Theta}_{D\boldsymbol{g}_3} + \boldsymbol{\Theta}_{D\boldsymbol{g}_3}^T \boldsymbol{\Theta}_{D\boldsymbol{g}_2} + \boldsymbol{\Theta}_{D^2\boldsymbol{g}_3}(\boldsymbol{g}_2)\right) \end{aligned}. \tag{37}$$

For the external virtual work (15) one has for the force contribution

$$\delta W_{ext} = \left[\boldsymbol{Q}\right]^T \boldsymbol{\Theta}_{D\boldsymbol{x}} \delta\boldsymbol{\Phi} \,, \tag{38}$$

$$\Delta\delta W_{ext} = \delta\boldsymbol{\Phi}^T \boldsymbol{\Theta}_{D^2\boldsymbol{x}} \Delta\boldsymbol{\Phi} \,. \tag{39}$$

The contribution of the moment is

$$\delta W_{ext} = \left[\boldsymbol{M}\right]^T \boldsymbol{\Theta}_{\delta\boldsymbol{\varpi}} \delta\boldsymbol{\Phi} \,, \tag{40}$$

$$\Delta\delta W_{ext} = \delta\boldsymbol{\Phi}^T \boldsymbol{\Theta}_{\Delta\delta\boldsymbol{\varpi}} \Delta\boldsymbol{\Phi} \,, \tag{41}$$

As explained in [26], the matrices $\boldsymbol{\Theta}_{D(\cdot)}$ and $\boldsymbol{\Theta}_{D^2(\cdot)}$ are symmetric, except $\boldsymbol{\Theta}_{\delta\boldsymbol{\varpi}}$ and $\boldsymbol{\Theta}_{\Delta\delta\boldsymbol{\varpi}}$, which are not symmetric due to the fact that the moment is not conservative.

The element tangent stiffness matrix is obtained from Eqs. (36), (39) and (41), the external force vector is obtained from (38) and (40), whereas the internal force vector follows from (34).

5. NUMERICAL EXAMPLES

5.1. Cantilever beam subjected to rotating tip loads

Consider the rectangular section cantilever beam shown in Figure 3, subjected to a free end centroidal force F = 100 kN. The force is first applied downwards (θ = 0), in a single step, and then its direction is changed by multiples of 45º, while the intensity is maintained. The beam is discretized with four equal-length finite elements and infinitesimal strains are considered, meaning that the proposed formulation may be compared with the Euler-Bernoulli model.

At each equilibrium configuration, the beam is subjected to simple bending. When the loading direction changes, the geodesic also changes and therefore torsion is generated in the

first equilibrium iteration. The figure shows the deformed configurations for each load increment and the evolution of the norm of the out-of-balance forces corresponding to M_3 and F only, designated by $\|\boldsymbol{T}\|$, with the accumulated number of iterations. Naturally, during the iterations of the first increment no torsion is generated, since all cross-sections are orientated along the same geodesic, and thus no values are shown in the graph for iterations 1 to 6. For the subsequent increments, torsion appears but decreases as the iterative process progresses. For all increments, a radial displacement of the tip equal to 3.00711803 m was obtained after six iterations.

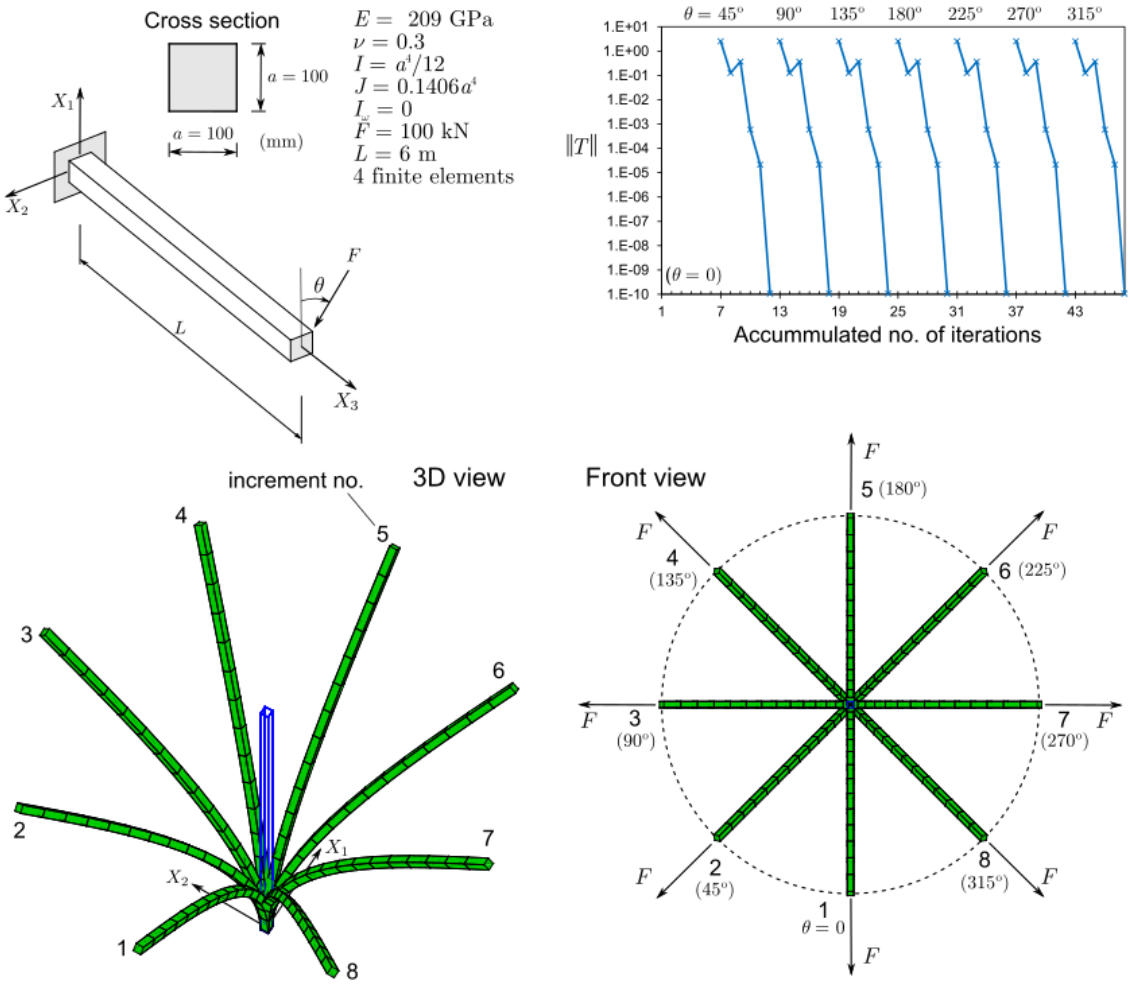

Figure 3: Cantilever subjected to a rotating tip force. The deformed configurations are obtained by subdividing each finite element into four segments.

Figure 4 shows the results obtained when a free end moment is applied instead. Once again, no torsion occurs in the first increment but is generated in the subsequent increments (and decreases as the corresponding iterations progress). For all increments, the radial displacement of the tip equals 3.51978061 m after seven iterations, which is very close to the Euler-Bernoulli solution (3.51984934 m). The bottom graph shows the error norm proposed in [19] as a function of uniform mesh refinement, for the first load increment. This norm reads

$$\| e \|^2 = \frac{1}{u_{\max}} \sqrt{\int_0^L \| \boldsymbol{r} - \boldsymbol{r}_{\text{ref}} \|^2 \, \mathrm{d}X_3} \,, \tag{42}$$

where $\boldsymbol{r}$ corresponds to the finite element solution, $\boldsymbol{r}_{\text{ref}}$ is the reference solution (Euler-Bernoulli) and $u_{\max}$ is its maximum displacement. The convergence rate is of order 4, as explained in [19].

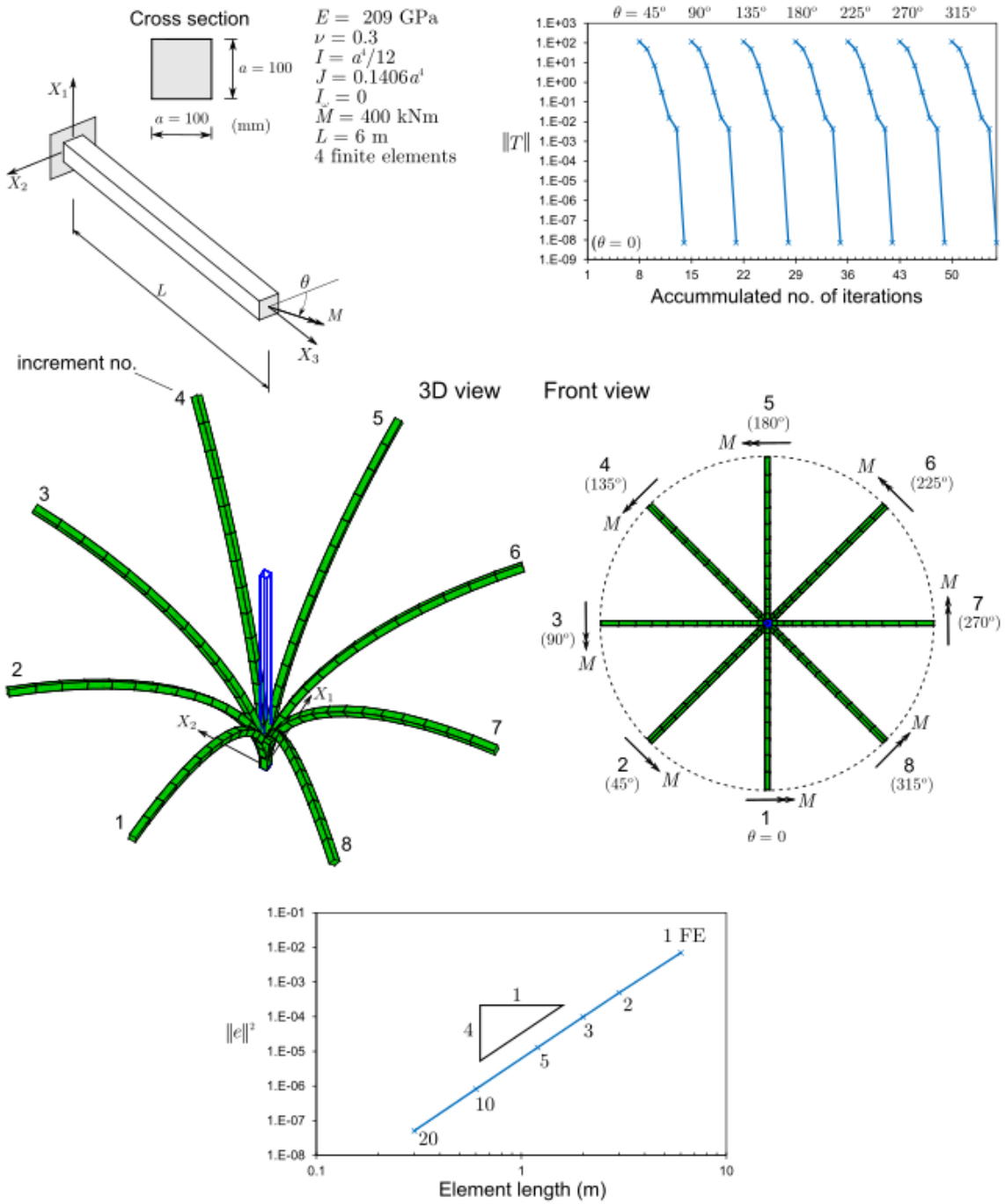

Figure 4: Cantilever subjected to a rotating tip moment. The deformed configurations are obtained by subdividing each finite element into four segments.

5.2. I-section under non-uniform torsion

This example was originally analyzed in [24] and is shown in Figure 5: an I-section cantilever is subjected to an imposed torsional twist at the free end. The built-in end constrains all displacements, including warping. For comparison purposes, the results obtained in [24] are

also shown in the figure, using eight equal-length two-node shear deformable geometrically exact beam finite elements based on shell-like membrane/bending stress resultants.

The cross-section is subdivided into three walls (two 100×15 flanges and one 185×10 web) and the following approximate warping function is adopted (calculated assuming thin walls)

$$\omega_{\text{top flange}} = X_1 X_2 - X_2 \bar{h}\,, \tag{43}$$

$$\omega_{\text{web}} = -X_1 X_2\,, \tag{44}$$

$$\omega_{\text{bottom flange}} = X_1 X_2 + X_2 \bar{h}\,, \tag{45}$$

where $\bar{h} = h - t_f$, with h = 215 mm and t_f = 15 mm.

The results show that, due to the Wagner effect (see, e.g., [22]), a non-uniform moment-rotation relation is retrieved and axial shortening of the beam occurs. Note that a single element already leads to very accurate results and. With 10 elements and an end rotation of π, the moment is only 1.5% lower than that obtained with one element and 1.0% below that of [24].

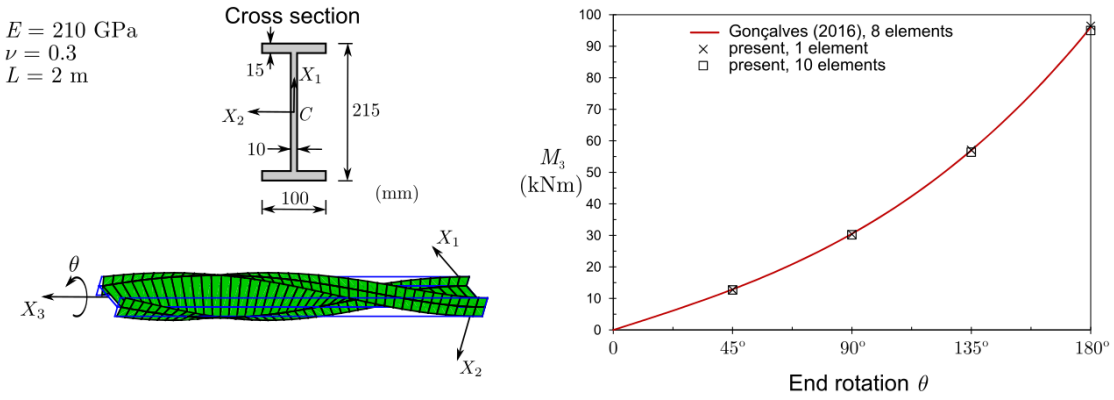

Figure 5: I-section cantilever subjected to a torsional twist. The deformed configuration corresponds to a discretization with 10 finite elements and is rendered using four subdivisions along each wall.

5.3. Lateral-torsional buckling of an I-section cantilever

Consider the I-section cantilever shown in Fig. 6, which undergoes lateral-torsional buckling. Besides the increasing free end shear centre force, a constant lateral perturbation force F_2 = –0.01 kN is introduced to enforce a slight imperfection.

With the proposed beam element, both infinitesimal and finite strain formulations are considered. For comparison purposes, the results obtained with a refined MITC-4 shell finite element model, analysed with ADINA [25], are also provided in the figure.

The load-displacement graph shown in the figure clearly evidences that the infinitesimal strain version (which does not allow for the Wagner effect) is very close to the shell model results up to 9 kN. Beyond this point only the finite strain formulation yields very accurate results, even when only six equal-length finite elements are employed. The deformed configurations shown in the bottom of the figure, further confirm the accuracy of the finite strain version of the proposed beam finite element.

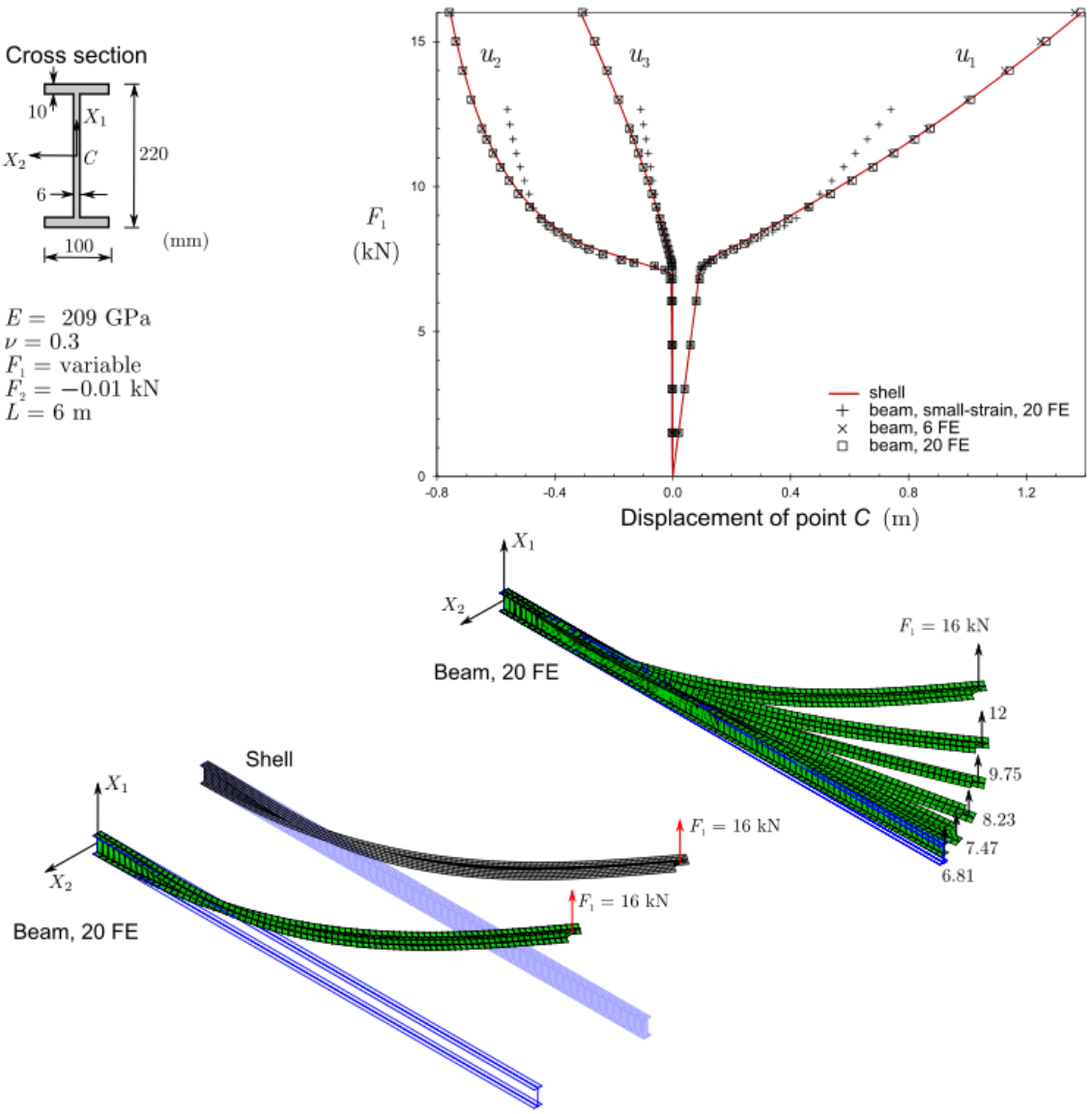

Figure 6: Lateral-torsional buckling of an I-section cantilever. For the beam deformed configurations, each element is subdivided into four segments.

5.4. Channel cantilever beam

Finally, the lateral-torsional buckling problem of a channel section cantilever, originally proposed in [8], is analyzed. The beam is subjected to a concentrated force, applied at point A of the free end cross-section, as displayed in Figure 7. This example was selected due to the fact that, for this cross-section, the centroid and shear centre do not coincide and the force is eccentric with respect to *C*. In Figure 7, the results obtained with the proposed beam finite element are compared with those in [8], obtained using 30 equal-length two-node beam elements[1], and also those obtained in [24], with 30 equal-length two-node shear deformable geometrically exact beam elements.

[1] In [8] it is shown that these results match very accurately those obtained with a shell finite element model involving 360 four-node elements.

With the proposed beam element, the cross-section is subdivided into three walls (two 100×16 flanges and one 268×10 web) and the following approximate warping function is adopted

$$\omega_{\text{top flange}} = X_2(X_1 - \bar{h}) - \bar{h}e\,, \tag{46}$$

$$\omega_{\text{web}} = -X_1(X_2 + 2e)\,, \tag{47}$$

$$\omega_{\text{bottom flange}} = X_2(X_1 + \bar{h}) + \bar{h}e\,, \tag{48}$$

where $\bar{b} = b - t_w/2$, $\bar{h} = h - t_f$, with b = 100 mm, h = 300 mm, t_f = 16 mm, t_w = 10 mm, and $e = 3\bar{b}^2/(6\bar{b} + \bar{h}t_w/t_w)$ stands for the distance between C and the web mid-line.

The graph in Figure 7 shows that using 10 equal-length elements already leads to results that practically match those obtained in [24], although for very large displacements the latter are very slightly above the ones originally presented in [8]. Increasing the number of elements to 30 improves slightly the results obtained for large displacements.

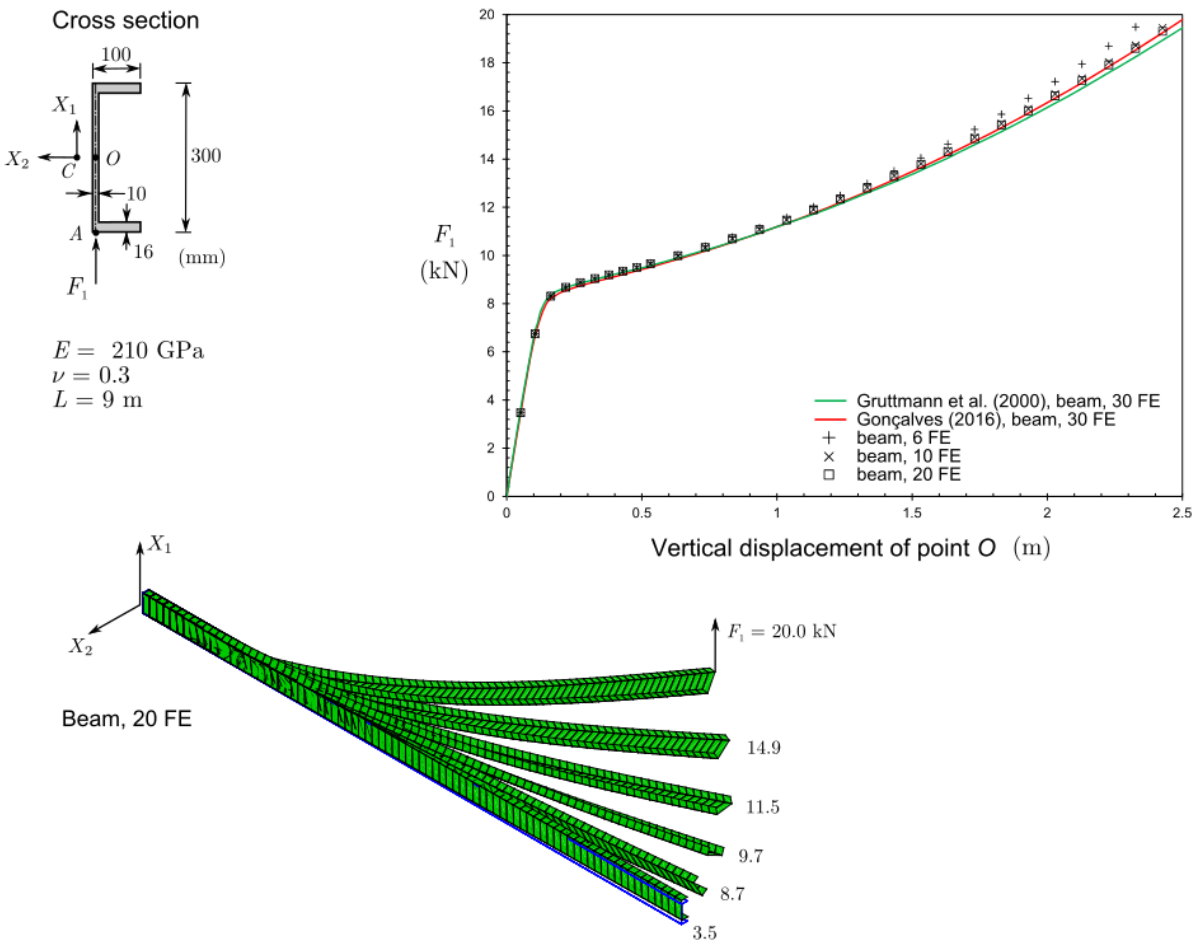

Figure 7: Channel cantilever beam. In the deformed configurations, each element is subdivided into four segments.

6 CONCLUSION

This paper presented a geometrically exact Kirchhoff beam model and the corresponding finite element implementation. The formulation employs the so-called "smallest rotation" parametrization of the cross-section orientation, whose treatment is far from trivial. Torsion-warping and Wagner effects are included, as well as force eccentricity effects and the possibility of considering cross-sections with non-coincident shear centre and centroid, to allow capturing the 3D large displacement behavior of thin-walled beams. The numerical examples presented clearly demonstrate the accuracy of the proposed beam finite element.

REFERENCES

[1] Boyer F. and Primault D., "Finite element of slender beams in finite transformations: a geometrically exact approach", *International Journal for Numerical Methods in Engineering*, **59**, 669-702, 2004.

[2] Reissner E., "On one-dimensional finite-strain beam theory: the plane problem", *Journal of Applied Mathematics and Physics*, **23**(5), 795-804, 1972.

[3] Reissner E., "On one-dimensional large-displacement finite-strain beam theory", *Studies in Applied Mathematics*, **52**, 87-95, 1973.

[4] Simo J.C., "A finite strain beam formulation. the three-dimensional dynamic problem, part I", *Computer Methods in Applied Mechanics and Engineering*, **49**, 55-70, 1985.

[5] Cardona A. and Geradin M., "A beam finite element non-linear theory with finite rotations", *International Journal for Numerical Methods in Engineering*, **26**(11), 2403-2438, 1988.

[6] Pimenta P.M. and Yojo T., "Geometrically exact analysis of spatial frames", *Applied Mechanics Reviews*, **46**(11S), 118-128, 1993.

[7] Ibrahimbegovic A., Frey F. and Kozar I., "Computational aspects of vector-like parametrization of three-dimensional finite rotations", *International Journal for Numerical Methods in Engineering*, **38**(21), 3653-3673, 1995.

[8] Gruttmann F., Sauer R. and Wagner W., "Theory and numerics of three-dimensional beams with elastoplastic material behaviour", *International Journal for Numerical Methods in Engineering*, **48**(12), 1675-1702, 2000.

[9] Ritto-Corrêa M., "Structural analysis of frames: towards a geometrically exact, kinematically complete and materially non-linear theory" (Ph.D. thesis), Lisbon Technical University, 2004 (In Portuguese).

[10] Gonçalves R., Ritto-Corrêa M. and Camotim D., "A large displacement and finite rotation thin-walled beam formulation including cross-section deformation", *Computer Methods in Applied Mechanics and Engineering*, **199**(23-24), 1627-1643, 2010.

[11] Gonçalves R., Ritto-Corrêa M. and Camotim D., "Incorporation of wall finite relative rotations in a geometrically exact thin-walled beam element", *Computational Mechanics*, **48**(2), 229-244, 2011.

[12] Weiss H., "Dynamics of geometrically nonlinear rods: I. Mechanical models and equations of motion", *Nonlinear Dynamics*, **30**(4), 357-381, 2002.

[13] Weiss H. "Dynamics of geometrically nonlinear rods: II. Numerical methods and computational examples", *Nonlinear Dynamics*, **30**(4), 383-415, 2002.

[14] Crisfield M., *Non-linear finite element analysis of solids and structures*, vol. 2, Wiley, 1997.

[15] Gonçalves R., "A geometrically exact approach to lateral-torsional buckling of thin-walled beams with deformable cross-section", *Computers and Structures*, **106-107**, 9-19, 2012.

[16] Gerstmayr J., Irschik H., "On the correct representation of bending and axial deformation in the absolute nodal coordinate formulation with an elastic line approach", *Journal of Sound and Vibration*, **318**(3), 461-487, 2008.

[17] Irschik H., Gerstmayr J., "A continuum mechanics based derivation of Reissner's large-displacement finite-strain beam theory: the case of plane deformations of originally straight Bernoulli-Euler beams", *Acta Mechanica*, **206**(1-2), 1-21, 2009.

[18] Gonçalves R. and Carvalho J., "An efficient geometrically exact beam element for composite columns and its application to concrete encased steel I-sections", *Engineering Structures*, **75**, 213-224, 2014.

[19] Meier C., Popp A. and Wall W.A., "An objective 3D large deformation finite element formulation for geometrically exact curved Kirchhoff rods", *Computer Methods in Applied Mechanics and Engineering*, **278**, 445-478, 2014.

[20] Simo J. and Vu-Quoc L., "A geometrically-exact rod model incorporating shear and torsion-warping deformation", *International Journal of Solids and Structure*, **27**(3), 371-393, 1991.

[21] Ritto-Corrêa M. and Camotim D., "On the differentiation of the Rodrigues formula and its significance for the vector-like parameterization of Reissner-Simo beam theory", *International Journal for Numerical Methods in Engineering*, **55**(9), 1005-1032, 2002.

[22] Pi Y.L., Bradford M.A. and Uy B., "A spatially curved-beam element with warping and Wagner effects", *International Journal for Numerical Methods in Engineering*, **63**(9), 1342-1369, 2005.

[23] Goldstein H., *Classical mechanics*, second ed., Addison-Wesley, 1980.

[24] Gonçalves R., "A shell-like stress resultant approach for elasto-plastic geometrically exact thin-walled beam finite elements", *Thin-Walled Structures*, **103**, 263-72, 2016.

[25] Bathe K.J., *ADINA system.*, ADINA R&D Inc., 2016.

[26] Manta D. and Gonçalves R., "A geometrically exact Kirchhoff beam model including torsion warping", *Computers and Structures*, **177**, 192-203, 2016.